Dynamics of the aortic root functional unit using Direct Numerical Simulation*

R. Verzicco[1,2] & M.D. de Tullio[3]

[1]DII, Universita di Roma "Tor Vergata", Roma, Italy
[2] PoF and MESA+, University of Twente, Enschede, The Netherlands
[3] DMMM, Politecnico di Bari, Bari, Italy

Abstract

The dynamics of the functional unit aortic valve/aortic root/coronary arteries/ascending aorta is very complex owing to the interaction of several mechanisms that interfere each other; this makes in vivo and in vitro analyses very expensive and numerical simulations a desirable option.

In this paper we describe an integrated tool that has been developed over the last decade capable of performing high-fidelity simulations which include the fluid/structure interaction, the deformability of the aortic wall and several other relevant features of the problem.

Some representative results are described in order to show the capabilities of the method.

1. Introduction

The replacement or re-modeling of heart valves, coronary arteries and aorta tracts is a relatively safe clinical practice, adopted whenever the actual organ cannot operate properly. Since the first successful heart valve replacement almost five decades ago, more than fifty valve designs have been developed and many others are being evaluated. Similarly, prosthetic aortic roots, biological and artificial bypass ducts and surgical procedures are continuously developed and tested (Sarsam & Yacoub, 1993; David & Feindel, 1992; Yacoub, 1996; David et al., 2001; Cochran et al., 1995; Bentall & De Bono, 1968; Karck et al., 2004; De Paulis et al., 2004; Weltert et al., 2009). The evaluation procedures include clinical trials, laboratory experiments (often called in vitro experiments) and more recently also numerical simulations.

Although many progresses have been obtained by studying the dynamics of single parts, it has been realized that they are elements of a more complex set-up and

* Der Vortrag wurde am 26.04.2013 anlässlich der Jahresversammlung der Braunschweigischen Wissenschaftlichen Gesellschaft gehalten.

considering the complete system would be desirable in order to obtain further improvements.

More in detail, among the four heart chambers, the left ventricle is the strongest and it ejects the blood into the aorta that, in turn, feeds the systemic circulation. The aortic valve is located just downstream of the left ventricle and before the aorta whose initial tract, the aortic root, shows a peculiar geometry. It is characterized by three sinuses (sinuses of Valsalva) and, from two of them, the coronary arteries originate. These small arteries have a great clinical relevance because they supply oxygenated blood to the myocardial muscle itself (Nichols & O'Rourke, 1990; Zamir, 2005). Beyond the aortic root there is the ascending aorta whose walls store tension under the effect of the blood pressure, ejected during the systolic phase, and gradually release it during the diastolic phase thus assuring a smooth flow. The operation of such a complex set requires the coordinated interaction of different systems and in fact the former is referred to as 'functional unit' that should be analyzed as a whole rather than split into separate components.

The development of a computational model for the complete system is therefore motivated by physical but also medical and economic concerns as well as efficiency (Borazjani et al., 2007; Dasi et al., 2007; Nobili et al., 2008; de Tullio et al., 2009; Sotiropoulos & Borazjani, 2009). Sufficiently accurate computational models, in fact, would serve as inexpensive tools for scientific and medical research that, combined with medical imaging and other cardiovascular diagnostic techniques, would provide fundamental information for the improvement of the patients care.

Despite the progress in numerical methods and the forever increasing power of modern computers, however, the problem is still very challenging since it is composed by different problems each of them tough in its own. The aortic valve, in fact, operates under the forces exerted by the flow while the latter, in turn, depends on the instantaneous geometrical configuration of the domain; this is a fluid/structure interaction problem that requires the coupled solution of the structure and flow dynamics. The flow is unsteady (pulsatile) and transitional thus requiring the accumulation of tens of flow cycles in order to compute reliable phase averages but, at the same time, the computation must be advanced with time steps small enough to capture the dynamics of the smallest turbulence structures. Equally problematic is the disparity of spatial flow scales that requires to account for large structures with a scale comparable to the valve orifice (27 mm) down to the Kolmogorov scale ($\simeq$ 30 μm); this requires a very fine spatial resolution over a computational domain big enough to accommodate few of the largest scales. In addition, the above dynamics must be computed in a very complex geometry with parts in relative motion and deforming boundaries.

In this paper we describe an attempt to model the complete functional-unit with a high-fidelity numerical model that, while accounting for all the most relevant

features of the problem, keeps the computational cost of the simulation at a reasonable level so to allow reliable numerical simulations without resorting to the large scale supercomputers.

In the next section we describe the main features of the model while the section of the Results illustrates some of the main achievements.

2. The problem

2.1 The equations

The model problem is sketched in figure 1 and it consists of an initial tract of a rigid pipe (mimicking the aorto-ventricular junction) where a mechanical bileaflef valve is mounted. Downstream of the valve there is the deformable aortic root from which the coronary arteries, also deformable, originate. After the aortic root there is the initial part of the ascending aorta that is modeled as a deformable cylindrical pipe.

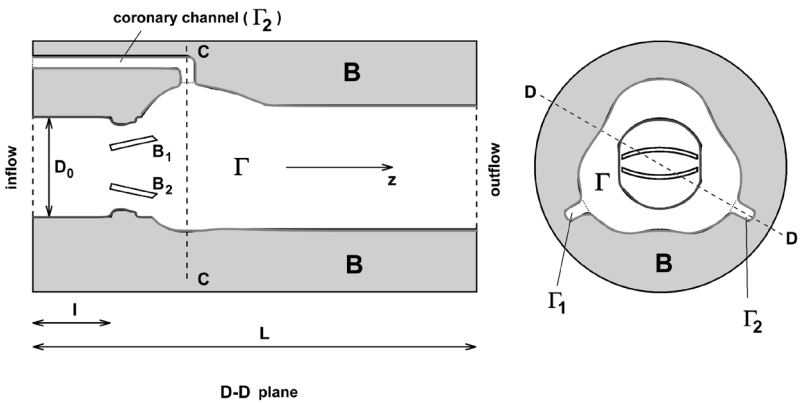

Fig. 1: Sketch of valve/root arrangement and computational domain ($L = 5D_0$; $l = D_0$)

In the time-dependent fluid domain $\Gamma + \Gamma_1 + \Gamma_2$ the Navier-Stokes equations for an incompressible viscous fluid are solved:

$$\begin{aligned} \frac{\partial \mathbf{u}}{\partial t} + \nabla \cdot (\mathbf{uu}) &= -\nabla p + \frac{1}{Re} \nabla \cdot \tau + \mathbf{f} + \mathbf{f}', \\ \nabla \cdot \mathbf{u} &= 0, \qquad \text{on } \Gamma + \Gamma_1 + \Gamma_2 \end{aligned} \tag{1}$$

where $\mathbf{u}$ is the velocity vector, p is the pressure, $\mathbf{f}$ is the direct forcing of the immersed boundary method (Fadlun et al., 2000), $\mathbf{f}'$ is the forcing term for the

coronary arteries (de Tullio et al., 2011b), both later specified, and *Re* is the Reynolds number. The viscous stress tensor is defined through $\boldsymbol{\tau} = 2\rho\nu(|\mathbf{E}|)\mathbf{E}$ and the kinematic viscosity of the fluid can be either constant $\nu(|\mathbf{E}|) = \nu_0$ or a function of the rate-of-strain tensor modulus $|\mathbf{E}|$: In the first case the fluid is Newtonian, in the second is non-Newtonian.

Among the various possibilities we have adopted for the blood the shear-thinning model of Carreau that reads

$$\nu(|\mathbf{E}|) = \nu_\infty + (\nu_0 - \nu_\infty)[1 + (\lambda \mid \mathbf{E} \mid)^2]^{(n-1)/2} \tag{2}$$

where and both λ and n are hematocrit dependent parameters. We have chosen the parameters for an adult healthy male with an hematocrit of 40% that yield for $\nu_\infty \simeq 3.7 \times 10^{-6}$ m^2/s high shear rates and $\nu_0 \simeq 4.3\nu_\infty$ for vanishing shear rates.

The two leaflets, $B_1$and B_2 can rotate about their own pivots and their angular displacements θ_i are governed by the following equations:

$$I_i \frac{\mathrm{d}^2\theta_i}{\mathrm{d}t^2} = T_i, \qquad \text{for } B_i \quad \text{with} \quad i = 1, 2, \tag{3}$$

where I_i are the dimensionless moment of inertia about the pivots and T_i are the tilting torques about the pivots resulting from the viscous stress tensor $\boldsymbol{\tau}$ and the pressure p integrated over the leaflets surfaces S_i. Their specific expressions are

$$T_i = \int_{S_i} [(\boldsymbol{\tau} \cdot \mathbf{n} - p\mathbf{n}) \times \mathbf{r}] \cdot \hat{x} \mathrm{d}S, \tag{4}$$

with $\mathbf{n}$ the outer normal to the surface S_i of the i-th leaflet, $\mathbf{r}$ the vector given by the distance from the pivot axis to the surface element dS and $\hat{x}$ the unit vector aligned with the pivot axis.

The deformable structures are governed by the Navier equation:

$$\nabla \cdot \sigma_s = \rho_s \frac{\partial^2 \mathbf{x}_s}{\partial t^2}, \tag{5}$$

where σ_s is the stress tensor, ρ_s the density and x_s the displacement of the solid. The constitutive and compatibility relations are:

$$\sigma_s = \mathbf{C}\mathbf{E}_s, \qquad \text{with} \qquad \mathbf{E}_s = \frac{1}{2}[\nabla \mathbf{x}_s + (\nabla \mathbf{x}_s)^T + (\nabla \mathbf{x}_s)^T \nabla \mathbf{x}_s], \tag{6}$$

being $\mathbf{C}$ the elasticity tensor and $\mathbf{E}_\mathrm{s}$ the strain tensor (de Tullio et al., 2011b).

The equations for the fluid are discretized in space using second-order-accurate central differences in conservative form. The large-banded matrix associated with the elliptic equation is reduced to a penta-diagonal matrix using trigonometric expansions (FFT's) in the azimuthal direction and the resulting Helmholtz equations are then inverted using the FISHPACK package (Swartzrauber, 1974). A third order Runge-Kutta scheme is used to advance the equations in time. All the simulations have been run with a fixed Courant number $CFL = 0.25$ thus having a variable time step Δt that is adjusted accordingly. Small time steps occur during opening and closing of the leaflets, thus allowing an accurate simulation of these phases, while larger time steps typically occur after valve closure, with a mean flow essentially zero and the leaflets still. More details on the Navier-Stokes solver are given in Verzicco & Orlandi (1996), and Fadlun et al. (2000). The immersed boundary technique used in this work is the same as that used in a previous work (de Tullio et al., 2009), based on that proposed by Fadlun et al. (2000), Iaccarino & Verzicco (2003) and Cristallo & Verzicco (2006).

2.2 Fluid/structure interaction

As mentioned previously, in a fluid/structure interaction problem the flow is determined by the structure dynamics that, in turn, depends on the fluid dynamic loads. It must be therefore decided if the fluid problem is solved first and then the structure is adjusted or if both problems must be solved together. The first approach is referred to as loose coupling and it can be used either when the structure undergoes small displacements or when the added mass effects are negligible. On the other hand, the coupled solution of the two systems is called strong coupling and, although computationally expensive, is more robust and allows the integration of virtually any fluid-structure interaction problem.

A strong coupling scheme is employed for the solution of the system (1)–(3) since the leaflet of the mechanical valve undergo very large rotations ($\simeq 60°$)and the added mass effects largely overcome the inertia of the leaflets. A Hamming's 4^{th}-order predictor-corrector method as described in Yang et al. (2008) is used to integrate equations (3) through an iterative scheme until convergence is achieved. In particular, equations (3) are expanded into a system of first order ordinary di erential equations in the variables θ_l , $\dot{\theta}_l$ with the generalized loads L_i on the right hand side. The fluid and structural solvers are then coupled through an iterative scheme and, for each time step, the number of iterations l is determined by the condition ei = $|\dot{\theta}_l^l - \dot{\theta}_l^{l-1}| < \varepsilon$. In all our computations a tolerance of $\varepsilon = 10^{-4}$ was used and the number of iterations required for convergence at each time step varied from 1 to 4, depending on the phase of the dynamics; convergence is typically more diffcult during the opening and closing phases when the leaflets rotate very rapidly while the criterion is satisfied already at the first iteration when the leaflets remain still or move slowly. In order to avoid numerical instabilities in the fluid-

structure interaction algorithm induced by the added mass effect due to the very low moment of inertia of the valve leaflets (Borazjani et al., 2007), we employed an under-relaxation of the generalized loads according to $L_i = \gamma L_i^l + (1\text{-}\gamma)L_i^{l\text{-}1}$ with $\gamma = 0.9$, l the actual iteration level and l-1 the previous one. Further details on the method and several checks of the numerics can be found in de Tullio et al. (2009).

Equations (5)–(6) are instead solved explicitly in time for the aortic root, the ascending aorta and coronary arteries. These structures, in fact, undergo only small displacements and therefore can be integrated using a loose coupling approach with the fluid. In this context the equations are advanced at the end of the time step with the local hydrodynamic loads on the structures and computed from the distributions of p and $\boldsymbol{\tau}$ obtained from equations (1); once the structure displacement $\mathbf{x}_s$ is obtained from (5)–(6) its velocity $\mathbf{u}_s$ can be computed and used as fluid boundary condition for the successive time step.

2.3 Immersed Boundary forcings

The forcing $\mathbf{f}$ in equation (1) is needed by the IB method in order to impose a velocity boundary condition over a surface that does not conform to coordinate lines. The great advantage of this approach is that it avoids the need of body-fitted meshes that, on geometrically complex and deforming geometries would require computationally demanding procedures. The actual need for an explicit computation of $\mathbf{f}$ depends on the particular IB technique, nevertheless every IB method eventually needs a reconstruction of the solution at the immersed surface. In fact, consider figure 2 where the shaded surface is the immersed boundary; it is immediately evident that while the boundary condition must be imposed over the surface, the flow unknowns are located somewhere in the computational cell and their position does not coincide with that of the surface; this is true for colocated methods as well as for staggered methods in which every flow variable is discretized in a different position. Simple mono- two- and full three-dimensional reconstruction schemes have been proposed (Fadlun et al. 2000, Gilmanov, Sotiropoulos & Balaras 2003, Tseng & Ferziger 2003, Kim et al. 2001) with different degrees of precision and effciency although all of them yielding a second-order accuracy.

One general procedure consists of a preliminary tagging of the computational cells which classifies the nodes into external, internal and interface points. The tagging can be performed by a ray-tracing algorithm (O'Rourke, 1998) as discussed in Iaccarino & Verzicco (2003) which is a standard in computer graphics. From each interface node (point A in figure 2) the normal to the immersed surface is drawn and the intersection W is computed. A tetrahedron is then constructed with A and the three closest external nodes (B, C and D) such that the point W is contained inside the tetrahedron. Every velocity component u_i (the same procedure could be used for other flow variables as density, temperature, scalar concentration, etc.)

is then computed in A in such a way that the same variable assumes the values in B, C and D computed from the governing equations without any forcing and the prescribed boundary condition in W. Within a linear reconstruction assumes the form:

$$u_i = ax + by + cz + d \tag{7}$$

with a, b, c and d and determined by the conditions $u_i = (u_i)_B$, $(u_i)_C$, $(u_i)_D$ and $(u_i)_W$, respectively, at the points B, C, D and W. Once the coefficients a, b, c and d and are known from the above conditions the value of u_i in A is simply given by $(u_i)_A = ax_A + by_A + cz_A + d$. If, instead of Dirichlet conditions, Neumann boundary conditions ($\partial u_i/\partial \mathrm{n} = \Phi_W$) are to be applied the wall condition $u_i = (u_i)_W$ is replaced by $\nabla u_i \cdot \mathbf{n} = \partial u_i/\partial x\alpha + \partial u_i/\partial y\beta + \partial u_i/\partial z\gamma = a\alpha + b\beta + c\gamma = \Phi_W$, where α, β and γ are the components of the normal $\mathbf{n}$ in W.

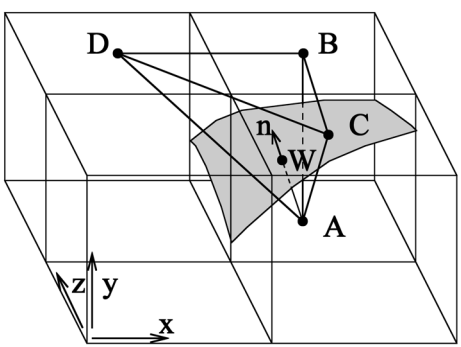

Fig. 2: Sketch of one possible interpolation scheme for the velocity reconstruction at the immersed boundary.

With the velocity vector $\mathbf{u}_A$ at hand, the forcing $\mathbf{f}$ for equation (1) is computed from its time-discrete version $(\mathbf{u}^{n+1} - \mathbf{u}^n)/\Delta t = \mathrm{RHS}^{n+1/2} + \mathbf{f}^{n+1/2}$ through

$$\mathbf{f}^{n+1/2} = \frac{\mathbf{u}_A - \mathbf{u}^n}{\Delta t} - \mathbf{RHS}^{n+1/2}, \tag{8}$$

which ensures $\mathbf{u}^{n+1} \equiv \mathbf{u}_A$ at the point A.

2.4 Modeling coronary-entry-flow

The ultimate function of the coronary system is to deliver blood to the cardiac tissue, that is alternately contracting and relaxing. During systole, the contrac-

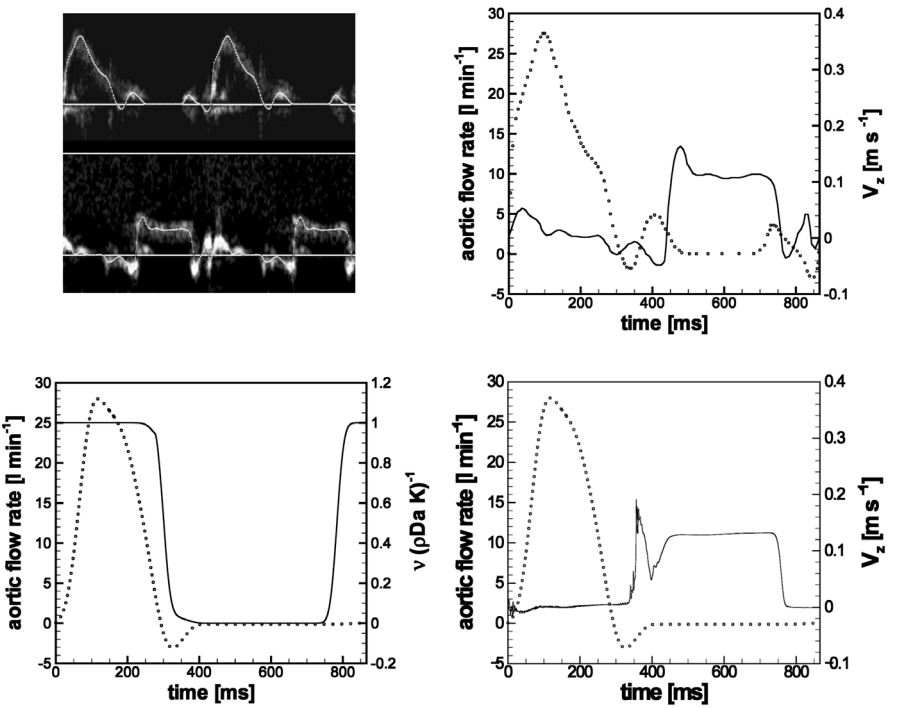

Fig. 3: (a) Aortic (upper) and coronaric (lower) velocity profiles by means of Pulse Wave Doppler echocardiography recorded in vivo in a young healthy man; (b) digitized aortic flow rate and mean coronaric velocity; (c) forcing term $\mathbf{f}'$ (9) inside coronaries in function of time; (d) computed average velocity in left (continuous line) and right (dashed line, almost invisible superimposed on the continuous line) coronary channel with diameter of D_c = 6 mm; the aortic flow (dotted line) is also reported for reference.

tion of the myocardium compresses the intra-myocardial capillaries, resulting in a *throttling* of these vessels. This effect ceases during diastole when the myocardium relaxes, and, although it is stretched by ventricular dilatation, the blood can better flow through the coronaries under the driving pressure gradient. This leads to a pulsatile flow in which the resistance can not be simply related to the vessel radius. In this model we concentrate only on the very early vasculature of the coronary system, namely the two vessels connected to the Valsalva sinuses, assuming that everything downstream maintains the same behavior for different aortic geometries. Therefore, by *coronary blood flow* we indicate the flow through such main vessels, entering the coronary system, that is the only flow reasonably accessible for measurements. We have replaced the complex branching structure of the vascular system by two identical cylindrical tubes connected to the coronary ostia of the aorta in the two sinuses of Valsalva (see figure 1). In this way, the entrance region of the coronary vessels is correctly modeled both in terms of diameter and posi-

tion with respect with sinuses. The pressure gradient between the entrance region and the outflow of the tubes provides the driving force for the coronary flow. In order to mimic the above mentioned *tissue pressure effect* (Kajiya et al., 1993), that is the rhythmic contractions of the myocardium within each pumping cycle, a momentum loss for the points inside the main coronary vessels tracts (Γ_1 and Γ_2) is provided, as done in a porous medium, by adding a time-variable extra forcing term in the Navier-Stokes equation:

$$\mathbf{f}' = \frac{\nu(\mathbf{u} - \mathbf{V_S})}{\rho Da K(t)}. \tag{9}$$

Here, $\mathbf{V_s}$ is the forced velocity inside the porous medium, $D_a = K_0/L^2$ is the Darcy number, with K_0 and L a reference permeability and reference length, respectively, and $K(t)$ is a new free time-dependent parameter that modulates the porosity. If $K(t) \to \infty$ the forcing vanishes and the standard Navier-Stokes equations are recovered: this is set during diastole, when the fluid is allowed to flow through coronaries. If $K(t) \to 0$ the forcing becomes dominant in the equation yielding $\mathbf{u} = \mathbf{V_s}$: by imposing $\mathbf{V_s} = 0$ the no-flux condition inside the coronaries is obtained during systole. The effect of the forcing (9) on the system (1) is exactly known only for the extreme values of K, none of which can be used in a computational code. Accordingly, a tuning was necessary in order to modulate the forcing between these two extrema in such a way to obtain a realistic coronary flow rate. More in detail, the forcing was tuned so to reproduce, for the setup with the ideal aortic root and a coronary diameter $D_c = 6$ mm, a physiological flow similar to that observed by Pulsed Wave Doppler echo-cardiographic recording in a human being (figure 3a). The flow profile in this individual, a young man, has been chosen as it corresponds, by an expert cardiology judgement, to the most typically observed flow profile found in normal healthy conditions. In particular, the tuning was necessary at early diastole (negative peak of flowrate) in order to limit the high velocity peak that the suddenly reduced resistance of the channels provides: after 330 ms, the slope of the forcing curve is changed, maintaining the forcing greater than zero for about 70 ms (see figure 3c). It is worth noting that in practice the value of K can not be ∞, therefore during systole the computed coronary flow rate is not exactly zero but always negligible when compared to the main flow rate. Once **f'** has been identified as in figure 3c it has been maintained identical in all other simulations in which other flow details than the coronary arteries have been modified.

2.5 Flow parameters and simulation details

We have assumed as main scaling quantities the inflow diameter $D_0 = 27$ mm and the bulk velocity at the peak inflow $U = 0.81$ m/s that with a blood kinematic viscosity $\nu = 3.04 \times 10^{-6}$ m^2/s yield a Reynolds number $Re = UD_0/\nu = 7200$. The basic time unit is given by $D_0/U = 33.3$ ms so that, given the heart cycle of 866 ms,

the Strouhal number is $St = D_0/UT \simeq 3.85 \times 10^{-2}$. The leaflets are made of pyrolytic carbon, with density of $\rho_l = 2000$ kg/m^3, whereas the blood density is $\rho_b = 1060$ kg/m^3. In dimensional units each leaflet has a rotational inertia of 7.947×10^{-9} kg m^2 that when scaled with $\rho_b D_0^5$ becomes $I_i = 2.77 \times 10^{-4}$, $i = 1\ 2$ used in equations (3).

The aortic root, the valve housing and the leaflets are discretized with unstructured triangular meshes (Stereo Lithography format, STL) and are embedded into the background cylindrical structured grid. In a previous work (de Tullio et al., 2009), at the same Reynolds numbers and in a similar configuration,three computational grids were tested in order to assess the grid independence of the results. It was found that the required resolution was achieved with a grid made of $193 \times 137 \times 250$ nodes (about 6.6 millions points) in the azimuthal, radial and axial directions, respectively. In the present paper, we use an even finer grid made of $217 \times 165 \times 250$ nodes (about 8.95 millions points) in order to have enough grid points and accurately resolve the boundary layers in the tiny coronary channels. The grid is uniform in the azimuthal and radial directions, while it is non-uniform in the axial direction and clustered near the valve, where rich vorticity dynamics is observed.

Twenty cardiac cycles are computed for all cases. Each cycle is discretized by a variable time step ranging, in dimensionless units D/U_0, from $\Delta t_{min} = 10^{-4}$, (about 3 μs) occurring at the flow rate peak, to a maximum value of $\Delta t_{max} = 7.5 \times 10^{-3}$, (about 250 μs) during the diastole. The CPU time for the computation of each complete cycle was equivalent to about 75 hours on a single P-IV processor, equipped with 2 Gb of RAM.

The inflow velocity profile is assigned by an hyperbolic tangent function with stretching parameter $\gamma = 60$ which yields a flat velocity distribution in the bulk and accommodates the no-slip boundary condition at the aortic wall within a layer of thickness $\lambda/D_0 = 1/\sqrt{Re} \simeq 1.2 \times 10^{-2}$. This velocity profile is modulated in time to mimic the physiological flow rate pro duced by the heart in the left ventricle (figure 3) similarly to what already done by Romano (2008) and de Tullio et al. (2009). The cycle duration was set at 866 ms, corresponding to about 70 beats/min (natural heart rate at rest). The mean flow rate was adjusted to about 5 l/min with a peak flow rate of about 28 l/min. These are typical physiological conditions under which an adult aortic valve operates.

3. Results

In several previous works (de Tullio et al., 2009, 2011b,a, 2012) detailed flow analyses for some configurations of the aortic root have been presented and validated against analogous flows and experiments available from the literature; readers are referred therein for more details. In the following, we only describe the key features of the flow.

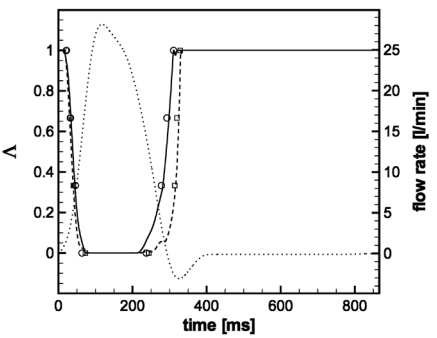

Fig. 4: Time variation of the phase-averaged leaflets angular position $\Lambda = \frac{(\alpha_{open}-\alpha)}{(\alpha_{open}-\alpha_{closed})}$ and flow rate (·····): comparison with experimental results (symbols) of Cerroni (2006). ---- and for □ leaflet B1 —— and ○ for leaflet B2.

Looking at figure 4, the leaflets dynamics can be summarized as follows: The opening phase (SO) starts at the beginning of the systole when the flow starts accelerating, and ends before the conclusion of the flow acceleration by reaching the fully open position (EO). The leaflets remain fully open during the peak of the flow rate curve (FP). The closing phase (SC) starts only at the beginning of the steepest flow deceleration and ends at the minimum (negative) of the flow rate by reaching the fully closed position (EC). From figure 4 it is evident that the valve is already fully open when the flow rate reaches about three-fourth of the peak value, and it maintains this configuration for slightly less than 20% of the pulsating period T. The opening phase of the valve lasts about 8% of T, while closing lasts approximately 14% of T and strongly depends on the temporal variation of the flow rate. In particular, the closing time depends on how steep is the flow-rate decrease, since it is related to the adverse pressure gradient that, in turn, determines the leaflets angular acceleration. It is worth mentioning that from preliminary simulations we have observed the opening of the leaflets to have little sensitivity to the waveform of the flow-rate increase while, in contrast, the closing phase was strongly dependent either on the slope of the flow rate descent or on the minimum value of the curve (regurgitation).

Figure 5 shows out-of-plane vorticity contours in the longitudinal plane containing one of the coronary channels (D – D plane of figure 1). The flow is sampled at four significant instants: (*i*) end opening of the leaflets; *ii*) flow rate peak; *iii*) start closure and *iv*) end closure of the leaflets clearly showing the small scale turbulence production from the instability of the shear layers released from the leaflets and valve housing.

At the beginning of the cycle (SO) the flow is essentially stagnant owing to the absence of mean flow for more than half period of the preceding cycle that has

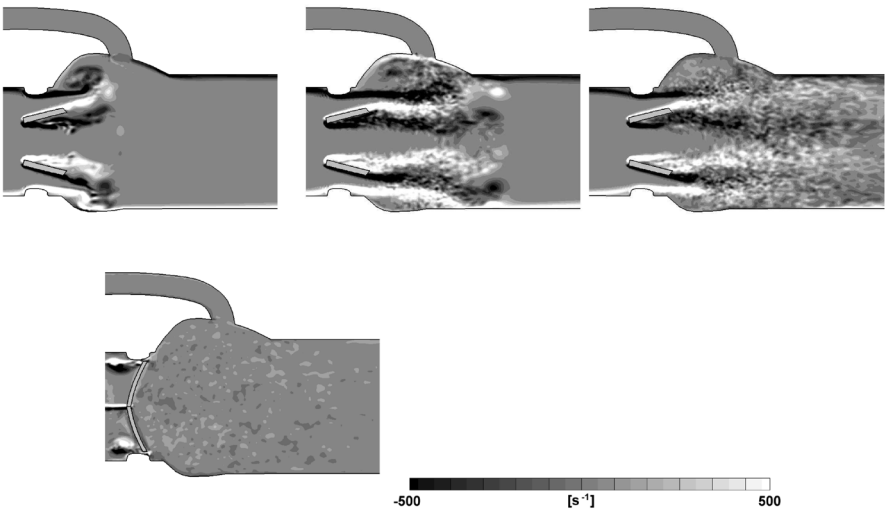

Fig. 5: Instantaneous out-of-plane vorticity contours in **D** – **D** plane at four significant instants (from top-right to bottom-left): end opening of the leaflets; flow rate peak; start closure; end closure of the leaflets.

allowed the turbulence to settle down; the residual vortical structures however are rapidly washed away by the incoming flow as the flow rate increases. During the early opening phase the leaflets start rotating to form a time-varying three-orifice configuration with strong shear layers shed from the valve housing, and the tips of the leaflets as shown by figure 5. After the leaflets reach the fully open position, the flow rate keeps increasing up to the peak value (FP), thus strengthening the shear layers that become unstable. The bulk of the flow however is still laminar owing to the flow acceleration that prevents turbulence from developing. At this stage the recirculations within the Valsalva sinuses have the maximum intensity, and the mean flow downstream of the valve has the distinctive three-jet signature. Though essentially laminar, the shear layers released from the leaflets have a strong flapping motion that further enhances the flow unsteadiness. This is especially true for the upper leaflet whose wake interacts with the recirculation in the sinus of Valsalva and starts a small-scale production leading to turbulence when the flow rate decreases and an adverse pressure gradient starts to develop. The valve starts closing when the flow rate is just above one-half of the peak value, and the instantaneous as well as the mean flow are asymmetric in the two leaflets. This asymmetry is reflected also by the pressure field which causes the lower leaflet to close before the other. As the flow rate also keeps decreasing, the upper leaflet closes and the fully closed position is attained at the negative peak of the flow rate. In this configuration, most of the flow leaks through the small gaps that mimic the washing of the hinges and some minor leakage occurs also from the gaps between

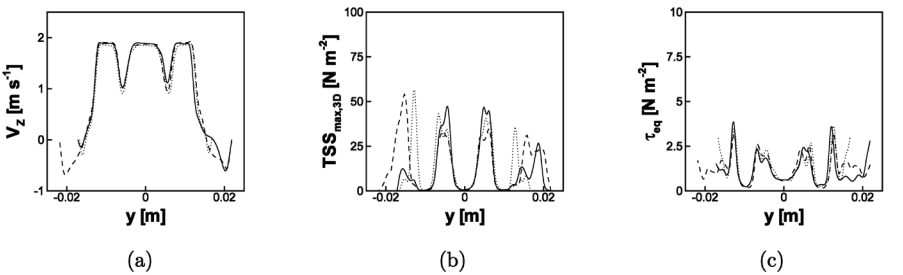

Fig. 6: Peak of flow rate: phase averaged streamwise velocity (a), maximum turbulent shear stress (b) and equivalent viscous stress (c) profiles in the plane of figure 1 in a section corresponding to the nadir of sinuses curvature. —— : three sinuses root; ---- : axisymmetric root; ···· : straight tube root.

the leaflets and between each leaflet and the valve housing. After this phase the turbulence in the bulk starts decaying owing to the absence of forcing provided by the mean flow and the decay continues up to the beginning of a new cycle.

Phase-averaged velocity profiles over twenty cardiac cycles have been computed, as well as maximum turbulent shear stress[1] and viscous stress[2] fields. Figure 6 reports the profiles of these fields in a section downstream of the valve, corresponding to the nadir of curvature of the sinuses. The data are sampled at the instant of the cycle corresponding to the flow rate peak ($t \simeq 140$ ms) in which the highest value of velocity is observed. In the panels we compare the profiles for three different configurations of the aortic root showing some differences only in the recirculation zone.

Figure 7 shows the pressure distribution at 366 ms, when the maximum coronary flow rate occurs; the total pressure difference is about about 15 mmHg showing little sensitivity to the particular aortic root geometry. Here we wish to stress that the IB method is capable to capture the highly localized pressure drop across the closed valve and the linear pressure decrease inside the coronary artery during its perfusion.

Another important result coming from these numerical simulations is the possibility to analyse and quantify the stresses induced on the structure by the fluid.

1 The maximum turbulent shear stress field is defined for each point by: $TSS^{3D}_{max} = (\sigma_1 - \sigma_3)/2$, where $\sigma_1$and σ_3 are the maximum and minimum principal shear stresses, obtained by the Reynolds stress tensor in the principal coordinate system and with a three-dimensional analysis (Popov, 1976; Malvern, 1977).

2 The reduction from the second-order viscous stress tensor to an equivalent scalar stress τ_{eq} has been performed according to the von Mises criterion used also by Apel et al. (2001). The expression of τ_{eq} is: $\tau_{eq} = \frac{1}{\sqrt{3}}\sqrt{\tau_{11}^2 + \tau_{22}^2 + \tau_{33}^2 - \tau_{11}\tau_{22} - \tau_{22}\tau_{33} - \tau_{11}\tau_{33} + 3(\tau_{12}^2 + \tau_{23}^2 + \tau_{13}^2)}$, where τ_{ij} are the viscous stress components.

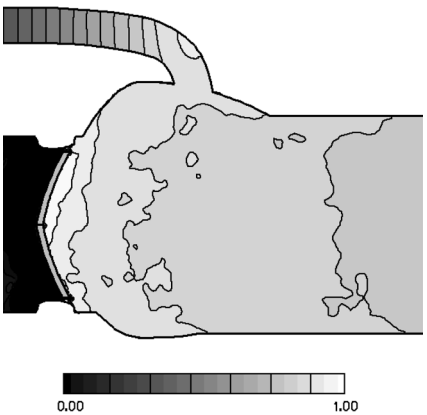

Fig. 7: Pressure distribution in the plane of figure 1 after valve closure: $\frac{p-p_{ref}}{\rho u_{ref}^2}$, where p_{ref} is the left ventricular pressure.

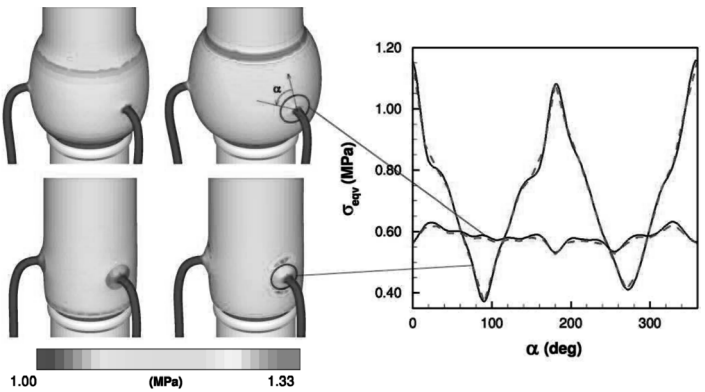

Fig. 8: Von Mises stress contours at minimum (left) and maximum (centre) levels of pressure during the cardiac cycle for the Valsalva (top) and straight pipe (bottom) aortic root. (Right) Von Mises stress in a circular region around the suture line.

This is particularly important either in biological tissues when some dilatation degeneration (aneurysm) is occurring and a prognostic information is needed or when a prosthetic device is implanted and the loads at the junctions between biologic and artificial tissues need to be evaluated. The latter case is particularly critical for the coronary arteries/aortic-root anastomoses whose bleeding is the major cause of surgery failure.

As an example of predictive capability of the present tool we show in figure 8 the surface stresses for two different geometrical configurations of the aortic root showing an advantage of the Valsalva-like one with respect to the straight tube.

4. Conclusions

In this paper, we have described a numerical tool for studying the pulsatile flow in the functional-unit aortic valve/aortic root/coronary arteries/ascending aorta with a realistic geometry so as to reproduce, as close as possible, the actual physiological conditions. This has been achieved by combining the immersed boundary method with a fluid-structure interaction algorithm that proved to be accurate and effcient. The main aim was to simulate the complete dynamics of the functional-unit without any compromise, either on the geometry of the system or on the flow physics. The results have been validated by a comparison with experimental data obtained for similar configurations (Cerroni, 2006; Romano, 2008); both the leaflets dynamics and the velocity fields are in satisfactory agreement, thus confirming the reliability of the numerical data. The main bottom line of this numerical tools is its inexpensiveness; first of all this technique does not need a body conformal mesh that, on account of the complex geometry with parts in relative motion, would imply a considerable computational overhead. In addition, the flow solver largely benefits from solutions on simple grids; the present simulations, in fact, could be carried out on grids in the range 6.6–10 millions of nodes using about 1.6×10^4 time steps per heart cycle within less than 2 Gb of RAM memory on a 3 GHz P-IV in about 75 h per cycle (single processor time equivalent).

Before concluding this paper we point out that the same package has been extensively used to investigate the phenomenon of hemolysis induced by the mechanical valve that requires the Lagrangian tracking of fluid particles and the evaluation of the stresses and their exposure time in oder to quantify the damage of the cell membranes; many details and results can be found in de Tullio et al. (2012).

Recent investigations have accounted for the non-Newtonian nature of the blood showing that, despite the common belief that blood behaves as a Newtonian liquid in large vessels this is not always true for the present problem De Vita et al. (2013). This turned out to be particularly true for the hemolysis that resulted increased by a 20% for the non-Newtonian model.

Finally, although in the present paper only mechanical valves have been presented, the model is already capable of handling biological valves with the leaflets that are deformable rather than rigid. This has been achieved by solving equations (5)–(6) also for the aortic valve although a substantial additional computational time was needed to account for the large displacements of the three deforming leaflets.

Acknowledgments

The help and advice of L. Afferrante, G. Pascazio, R. De Paulis, L. Weltert and E. Balaras is gratefully acknowledged by the authors.

References

Apel, J., P. Reinhard, S. Klaus, T. Siess & H. Reul 2001: Assessment of hemolysis related quantities in a microaxial blood pump by computational fluid dynamics. Artificial Organs **25**(5), 341–347.

Bentall, H. & A. De Bono 1968: A technique for complete replacement of the ascending aorta. Thorax **23**, 338–339.

Borazjani, I., L. Ge, P.L. Dasi, F. Sotiropoulos & A.P. Yoganathan 2007: Fluid-structure interaction in bi-leaflet mechanical heart valves. In *2nd Frontier in Biomedical Devices Conference*. June 7–8, California, USA, BioMed 2007-3807.

Cerroni, G. 2006: Studio sperimentale del campo fluidodinamico a valle di una valvola cardiaca artificiale e in un dispositivo di circolazione assistita mediante tecnica PIV. Master's thesis, Universita' degli studi di Roma, La Sapienza, Facolta' di Ingegneria.

Cochran, R.P., K.S. Kunzelman, A.C. Eddy, B.O. Hofer & E.D. Verrier 1995: Modified conduit preparation creates a pseudosinus in an aortic valvesparing procedure for aneurysm of the ascending aorta. The Journal of Thoracic and Cardiovascular Surgery **109**, 1049–1058.

Cristallo, A. & R. Verzicco 2006: Combined immersed boundary/large-eddy-simulations of incompressible three dimensional complex flows. Flow, Turbulence and Combustion **77**, 326.

Dasi, L.P., L. Ge, H.A. Simon, F. Sotiropoulos & A. Yoganathan 2007: Vorticity dynamics of a bilea et mechanical heart valve in an axisymmetric aorta. Physics of Fluids **19**, 1–17.

David, T.E., S. Armstrong, J. Ivanov, C.M. Feindel, A. Omran & G. Webb 2001: Results of aortic valve-sparing operations. The Journal of Thoracic and Cardiovascular Surgery **122**, 39–46.

David, T.E. & C.M. Feindel 1992: An aortic valve-sparing operation for patients with aortic incompetence and aneurysm of the ascending aorta. The Journal of Thoracic and Cardiovascular Surgery **103**, 617–622.

De Paulis, R., F. Tomai, F. Bertoldo, A.S. Ghini, R. Scaffa, P. Nardi & L. Chiarello 2004: Coronary flow characteristics after a Bentall procedure with or without sinuses of Valsalva. European journal of cardio-thoracic surgery **26**, 66–72.

De Vita, F., M.D. de Tullio & R. Verzicco 2013: Numerical simulation of the blood flow in the aortic root with a non-newtonian fluid model. In AIMETA Conference 2013, Torino, Italy., pp. 1–8. AIMETA.

Fadlun, E.A., R. Verzicco, P. Orlandi & J. Mohd-Yosuf 2000: Combined immersed-boundary finite-di erence methods for three-dimensional complex flow simulations. J. Comput. Phys. **161**, 35.

Iaccarino, G. & R. Verzicco 2003: Immersed boundary technique for turbulent flow simulations. Appl. Mech. Rev. **56**, 331.

Kajiya, F., S. Matsuoka, Y. Ogasawara, O. Hiramatsu, S. Kanazawa, Y. Wada, S. Tadaoka, K. Tsujioka, T. Fujiwara & M. Zamir 1993: Velocity profiles and phasic flow patterns in the non-stenotic human left anterior descending coronary artery during cardiac surgery. Cardiovascular Research **27**, 845–850.

Karck, M. K. Kallenbach, C. Hagl, C. Rhein, R. Leyh & A. Haverich 2004: Aortic root surgery in marfan syndrome: Comparison of aortic valve-sparing reimplantation versus composite grafting. The Journal of Thoracic and Cardiovascular Surgery **127**, 391–398.

Malvern, L.E. 1977: Introduction to the Mechanics of a Continuous Medium. Englewood Cliffs, Prentice Hall Inc.

Nichols, W.W. & M.F. O'Rourke 1990: McDonald's blood flow in arteries. Lea & Febiger, Philadelphia, PA.

Nobili, M., U. Morbiducci, R. Ponzini, C. Del Gaudio, A. Balducci, M. Grigioni, F.M. Montevecchi & A. Redaelli 2008: Numerical simulation of the dynamics of a bilea et prosthetic heart valve using a fluid-structure interaction approach. Journal of biomechanics **41**, 2539–2550.

Popov, E.P. 1976: Mechanics of materials, 2nd ed.. Englewood Cliffs, Prentice Hall Inc.

Romano, G.P. 2008: Deliverable d24-study case report n 2 pulse duplicator with aortic root model from rwth aachen smart-piv ist-2002-37548 european project. http://www.smart–piv.com.

Sarsam, M.A. & M. Yacoub 1993: Remodeling of the aortic valve anulus. The Journal of Thoracic and Cardiovascular Surgery **105**, 435–438.

Sotiropoulos, F. & I. Borazjani 2009: A review of the state-of-the-art numerical methods for simulating flow through mechanical heart valves. Medical & Biological Engineering & Computing **47**, 245–256.

Swartzrauber, P.N. 1974: A direct method for the discrete solution of separable elliptic equations. SIAM J. Numer. Anal. **11**, 113–150.

de Tullio, M.D., L. Afferrante, G. Demelio, G. Pascazio & R. Verzicco 2011a: Fluid-structure interaction of deformable aortic prostheses with a bilea et mechanical valve. J. of Biomechanics **44**, 1684–1690.

de Tullio, M.D., A. Cristallo, E. Balaras & R. Verzicco 2009: Direct numerical simulation of the pulsatile flow through an aortic bilea et mechanical heart valve. Journal of Fluid Mechanics **622**, 259–290.

de Tullio, M.D., J. Nam, G. Pascazio, E. Balaras & R. Verzicco 2012: Computational prediction of mechanical hemolysis in aortic valved prostheses. Eur. J. of Mech. B/fluids **35**, 47–53.

de Tullio, M.D., G. Pedrizzetti & R. Verzicco 2011b: On the e ect of the aortic root geometry on the coronary entry-flow after a bilea et mechanical heart valve implant: a numerical study. Acta Mechanica **216**, 147–163.

Verzicco, R. & P. Orlandi 1996: A finite di erence scheme for threedimensional incompressible flows in cylindrical coordinates. Journal of Computational Physics **123**, 402–413.

Weltert, L., R. De Paulis, R. Scaffa, D. Maselli, A. Bellisario & S. D'Alessandro 2009: Re-creation of a sinuslike graft expansion in Bentall procedure reduces stress at the coronary button anastomoses: A finite element study. Journal of thoracic and cardiovascular surgery **137**, 1082–1087.

Yacoub, M.H. 1996: Valve-conserving operation for aortic root aneurysm or dissection , pp. 57–67. Philadelphia: WB Saunders.

Yang, J., S. Preidikman & E. Balaras 2008: A strongly-coupled embedded boundary method for fluid-structure interaction of elastically mounted rigid bodies. J. Fluids and Structures **182**, 167–182.

Zamir, M. 2005: The Physics of Coronary Blood Flow. Springer.